

# We are IntechOpen, the world's leading publisher of Open Access books Built by scientists, for scientists

6,900

Open access books available

186,000

International authors and editors

200M

Downloads

Our authors are among the

154

Countries delivered to

TOP 1%

most cited scientists

12.2%

Contributors from top 500 universities



WEB OF SCIENCE™

Selection of our books indexed in the Book Citation Index  
in Web of Science™ Core Collection (BKCI)

Interested in publishing with us?  
Contact [book.department@intechopen.com](mailto:book.department@intechopen.com)

Numbers displayed above are based on latest data collected.  
For more information visit [www.intechopen.com](http://www.intechopen.com)



# Design and Optimization of Inductive Power Link for Biomedical Applications

Kejie Huang<sup>1,2</sup>, Yin Zhou<sup>1,3</sup>, Xiaobo Wu<sup>3</sup>, Wentai Liu<sup>4</sup> and Zhi Yang<sup>1,4</sup>

<sup>1</sup>*Department of Electrical and Computer Engineering, National University of Singapore*

<sup>2</sup>*Data Storage Institute, Agency of Science, Technology and Research*

<sup>3</sup>*Institute of VLSI Design, Zhejiang University*

<sup>4</sup>*Department of Electrical Engineering, University of California at Santa Cruz*

<sup>1,2</sup>*Singapore,*

<sup>3</sup>*China,*

<sup>4</sup>*USA*

## 1. Introduction

Powering biomedical devices is a major issue in the design of wearable and implantable electronics Chaimanonart et al. (2006); Chen et al. (2009); Kendir et al. (2004); Smith et al. (2002). Often, there is not space available for a battery that will last for the lifetime of the device, as batteries are limited both by total charge storage ability and number of recharge cycles Heller (2006). Replacement is often not an option, as the implant surgeries are both time consuming, require special expertise, and introduce the possibility of additional trauma to the patient. Percutaneous physical links Galbraith et al. (2007); Knutson et al. (2002) are prone to damage, because of the mismatch in material properties, scarring at the tissue interface Takura et al. (2006), and potential infections and skin irritation. In addition, these devices are difficult to keep sterile.

An alternative is inductive links, which are coupled coils forming an air core transformer Hamici et al. (1996); Li et al. (2005); Liu et al. (2000); Sauer et al. (2005); Sivaprakasam et al. (2005); Theogarajan & Wyatt (2006); Wang, Liu, Sivaprakasam, Weiland & Humayun (2005). As diagrammed in Fig. 1, an inductive link consists of two components of electronics. Those located externally or physically detached from the subjects are referred as primary side electronics, e.g., external battery, power transmitter, power control units, etc. Those located under the skin (implanted electronics) or along with the subjects (wearable electronics) are referred as secondary electronics, including resonant amplifier, rectifier, regulators, and power management units. Power-transmission efficiency and system miniaturization are major design specifications to evaluate a power link. Given application related constraints, these specifications are inherently correlated and a careful trade-off analysis is required to achieve an optimal performance.

This chapter is organized as follows. In Section 2, an introduction on power telemetry electronics is presented, followed by design analysis and simulation verifications. Section 3 focuses on inductor modeling, which correlates power efficiency with device size. Section 4 gives examples to quantify the achievable efficiency given design constraints.

## 2. Power telemetry electronics

### 2.1 Overview

The block diagram of an inductive power link is shown in Fig. 1 Kendir et al. (2005); Wang, Liu, Sivaprakasam & Kendir (2005). It consists of an external power supply, power amplifier, receiver resonant amplifier, inductive link and rectifier. The overall power load of secondary electronics are treated as a constant resistor for analysis.

Power efficiency of a telemetry link is defined as the ratio of the power consumed by load over the power derived from the battery. It is a most important parameter for performance evaluation. A second important parameter is the geometry size of the power receiver, where an inductor is the component of the largest footprint. In other words, a critical task in system miniaturization is to reduce the geometry size of the inductor used. In the rest of this section, modeling and analysis of individual circuit blocks are presented according to its relevance to power efficiency and device size.

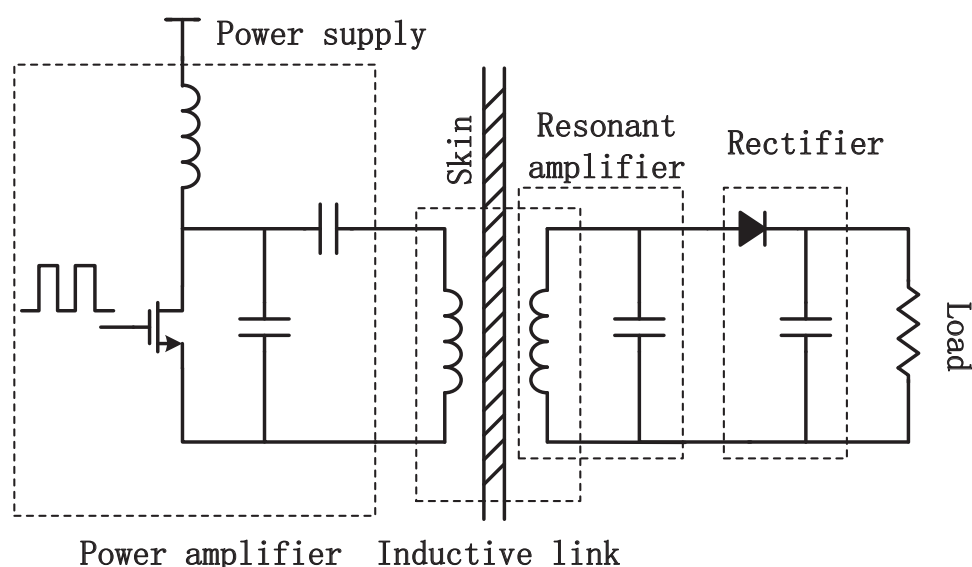


Fig. 1. Block diagrams of a generic inductive power telemetry link.

### 2.2 Power amplifier

There are different architectures available for building a power amplifier that converts a DC voltage to AC. Among the different designs, we choose Class-E power amplifier, because it achieves the highest power efficiency and suitable for implementation Kazimierczuk & Jozwik (2002); Sokal (2001). Compared with popular Class-D and Class-F amplifiers, it eliminates the power loss caused by shoot-through currents and achieves high impedance at harmonics Raab (2002).

As shown in Fig. 2, a class-E amplifier consists of two blocks: 1) a switching device and 2) an impedance network. The switch periodically turns on and off at the "zero-voltage" and "zero-current" point to avoid switching power losses. In practice this condition may not be 100% satisfied especially at a higher switching frequency, requiring careful tuning. The impedance network, on the other hand, is set up to attain resonance by minimizing the imaginary part of the impedance. The loading  $R_{load}$  consists of two part: equivalent series

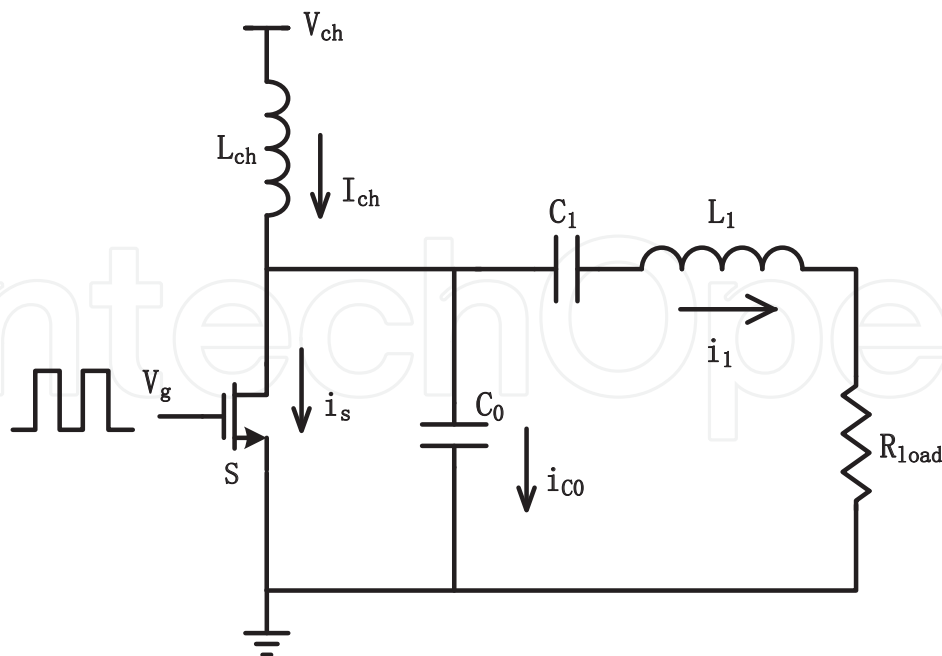


Fig. 2. Schematic of class E amplifier.

resistance(*ESR*) of inductor  $L_1$  and the reflected resistance due to inductive link which will be discussed in detail in Section 2.3.

Several assumptions of Class-E power amplifier are made to facilitate further analysis Krauss et al. (1980); Rogers et al. (2010).

1.  $L_{ch}$  is large enough to ignore current ripples on  $I_{ch}$ .
2. Frequency harmonics are removed by the loop filter  $L_1$  and  $C_1$ .
3. The variation in drain-to-source capacitor of the switch  $S$  is negligible compared with  $C_0$ .
4. "Zero voltage" turn on and "zero current" turn off conditions are precisely satisfied.

For illustration, we further assume switch  $S$  has a 50% duty cycle and is turned on at time  $(2n + 1)\pi$ . Under such conditions, closed-loop form expressions can be obtained.

The upper traces in Fig. 3 depict four crucial waveforms of Class E amplifier: the straight line  $I_{ch}$  is the DC current across  $L_{ch}$ .  $i_1$  represents the current in the resonant tank and is expressed as  $i_1 = I_1 \sin(\omega t + \phi)$ . The solid curve,  $i_s$ , and dotted curve,  $i_{C_0}$  are the currents flowing through the switch  $S$  and capacitor  $C_0$ , respectively. Note that  $i_s$  and  $i_{C_0}$  together make up a complete sinusoidal wave. The lower half of Fig. 3 gives the switch control signal  $V_g$  and drain to source voltage  $v_{C_0}$ .  $V_g$  forces the amplifier swapping between two alternative states: when  $S$  is on,  $i_s$  flows across the switch that shorts  $C_0$ ; when  $S$  is off,  $i_{C_0}$  charges up the  $C_0$ . The current flowing through  $C_0$  is

$$i_{C_0}(t) = \begin{cases} I_{ch} - I_1 \sin(\omega t + \phi), & 0 < \omega t < \pi \\ 0, & \pi < \omega t < 2\pi. \end{cases} \quad (1)$$

When the amplifier reaches its steady state, the voltage across  $C_0$  is

$$v_{C_0}(t) = \frac{1}{C_0} \int i_{C_0}(t) dt = \begin{cases} \frac{1}{\omega C_0} (I_{ch} * \omega t + I_1 \cos(\omega t + \phi) - I_1 \cos \phi), & 0 < \omega t < \pi \\ 0, & \pi < \omega t < 2\pi \end{cases} \quad (2)$$

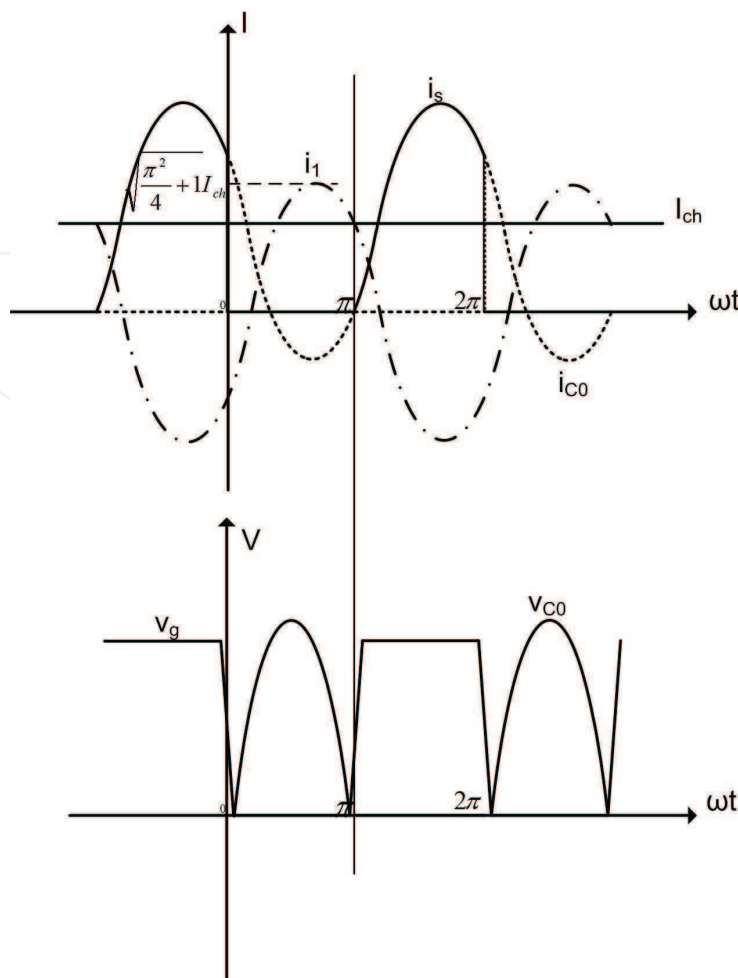


Fig. 3. Class E amplifier waveform when switch  $S$  has a 50% duty cycle and is turned on at time  $(2n + 1)\pi$

As reinforced conditions to further reduce switching power loss, Zero Differential Voltage Switching (ZDVS) and Zero Voltage Switching (ZVS) are added in designs Raab (1977).

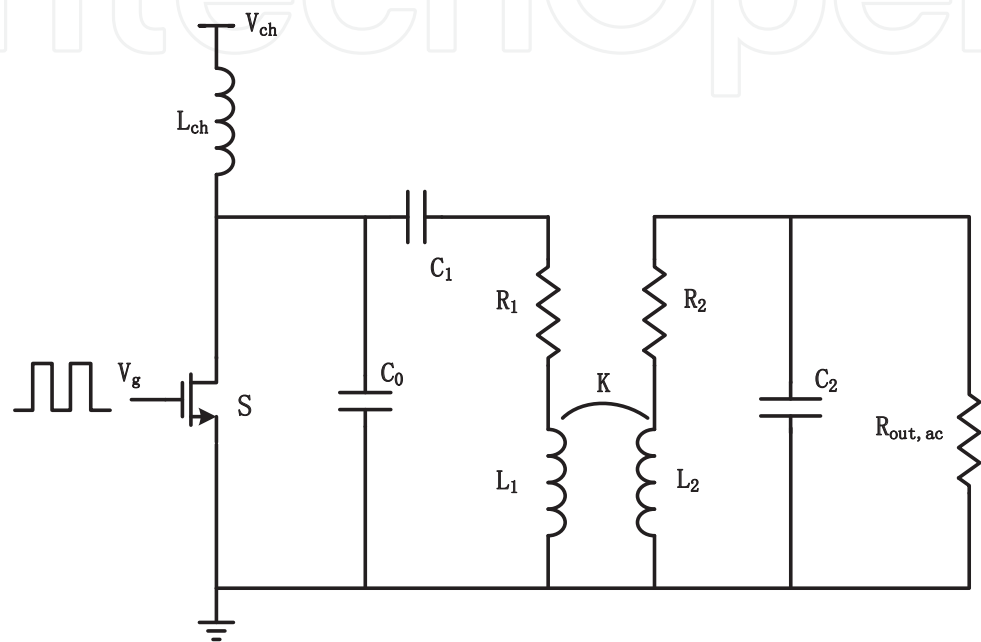
$$\frac{dv_{C_0}(t)}{dt}\bigg|_{t=\frac{T}{2}-} = 0, \quad v_{C_0}(t)\bigg|_{t=\frac{T}{2}-} = 0. \quad (3)$$

Equation 1 to 3 serve as key equations which prescribe a set of constraints for Class-E amplifier.

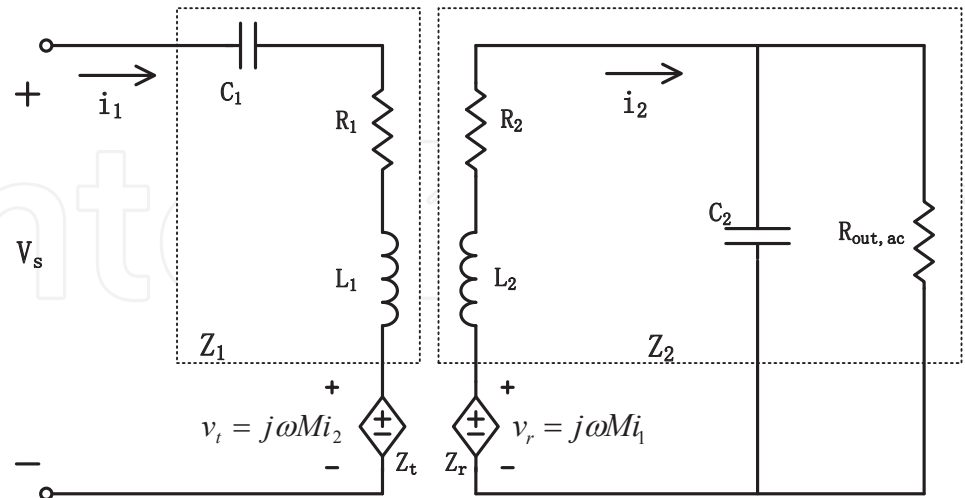
- Given the duty cycle, the relationship between the choke current ( $I_{ch}$ ) and oscillation current across the inductor ( $i_1$ ) is decided and can be numerically calculated by adding the turn on and turn off conditions. For example, when the duty cycle is 50%,  $\phi \approx -32.5^\circ$ ,  $I_1/I_{ch} = a = \sqrt{\frac{\pi^2}{4} + 1}$ , the equivalent input DC impedance is  $R_{in,dc} = (\frac{\pi^2}{8} + \frac{1}{2})R_{load}$ .
- The peak voltage across the switch ( $V_{peak}$ ) appears when  $dv_{C_0}(t)/dt = 0$  where  $V_{peak} \approx -2\pi\phi V_{ch}$ . The switch is required to be able to tolerate drain-to-source voltage drop several times higher than supply voltage;
- Once amplifier reaches a steady state, the averaged voltage across the switch is  $V_{ch}$ , making the choice of  $C_0$  sensitive to the duty cycle and tank load. The larger the turn off duty cycle

or tank load, the smaller  $C_0$  should be and the more sensitive to parasitic capacitance. As a first order estimation, when duty cycle is 50%,  $C_0 = 2/\omega R_{Load} a^2 \pi = 2Q_{system}/\omega^2 a^2 \pi L$ .

- The resonant tank is desired to have the peaked system Q at the operating frequency typically in sub-MHz or MHz range. If lower the frequency too much, the resonant tank becomes inefficient due to reduced inductor Q and large components values. If increase the frequency to GHz, the switching power loss and frequency related effects (detailed in Section 3), would significantly degenerate the power efficiency.



(a) Schematic of inductive power Link



(b) Equivalent model as an ideal transformer

Fig. 4. Inductive power link schematic and its equivalent circuit

### 2.3 Inductive link

Power efficiency is one of the major specifications for evaluating the performance of an inductive link Atluri & Ghovanloo (2005); Harrison (2007); Zierhofer & Hochmair (2002). In this section, emphasis is made to derive a set of analytic formulas to quantify a power telemetry efficiency, followed by discussions on performance optimization.

Fig. 4(a) illustrates a generic inductive power link, where  $R_1$  and  $R_2$  are *ESR* of inductor  $L_1$  and  $L_2$ .  $R_{out,ac}$  represents equivalent AC load resistance, which is half of its DC counterpart Ko et al. (1977). An equivalent model is shown in Fig. 4(b) Baker & Sarpeshkar (2007), where  $K$  is the coupling coefficient between  $L_1$  and  $L_2$ , and  $M = K\sqrt{L_1 L_2}$  is the mutual inductance. As the reflected impedance from the receiver and transmitter,  $Z_t$  and  $Z_r$  are

$$\begin{cases} Z_t = \frac{v_t}{i_1} = \frac{\omega^2 M^2}{Z_2} \\ Z_r = \frac{v_r}{i_2} = j\omega M \frac{i_1}{i_2} \\ Z_1 = R_1 + j\omega L_1 + \frac{1}{j\omega C_1} \\ Z_2 = R_2 + j\omega L_2 + \frac{1}{j\omega C_2} \parallel R_{out,ac} \end{cases} \quad (4)$$

where  $Z_1$  and  $Z_2$  are the impedance network shown in Fig. 4(a).

The transmitter efficiency (defined as the ratio of power consumed by the secondary electronics over the total power drained from a battery) and the receiver efficiency (defined as the ratio of power consumed by the load  $R_{out,ac}$  over the total power consumed at the receiver side) are

$$\begin{cases} \eta_1 = \left| \frac{Z_t}{Z_1 + Z_t} \right| \leq \frac{K^2 Q_1 Q_2 R_{out,ac}}{K^2 Q_1 Q_2 R_{out,ac} + Q_2^2 R_2 + R_{out,ac}} \\ \eta_2 = \left| 1 - \frac{R_2}{Z_2} \right| \leq \frac{Q_2^2 R_2}{Q_2^2 R_2 + R_{out,ac}} \end{cases} \quad (5)$$

where  $\eta_{1,2}$  reach its maximum if  $Z_{1,2}$  has only real part left;  $Q_1$  and  $Q_2$  are quality factors of external and internal coils, respectively.

The total efficiency is product of  $\eta_1$  and  $\eta_2$

$$\begin{aligned} \eta_{link} &= \eta_1 * \eta_2 \\ &\leq \frac{K^2 Q_1 Q_2^3 R_2 R_{out,ac}}{(K^2 Q_1 Q_2^3 R_2 R_{out,ac} + K^2 Q_1 Q_2 R_{out,ac}^2 + Q_2^4 R_2^2 + 2Q_2^2 R_2 R_{out,ac} + R_{out,ac}^2)} \\ &= \frac{1}{1 + X}, \text{ where} \\ X &= \frac{R_{out,ac}}{Q_2^3 Q_1 K^2 R_2} + \frac{R_{out,ac}}{Q_2^2 R_2} + \frac{2}{Q_2 Q_1 K^2} + \frac{R_2}{R_{out,ac} K^2 Q_1 / Q_2} \end{aligned} \quad (6)$$

where  $\eta_{link}$  reaches its maximum if both  $\eta_1$  and  $\eta_2$  reach their maximums at the carrier frequency. In other words, the values of  $L_1$ ,  $L_2$ ,  $C_1$  and  $C_2$  must be carefully chosen to ensure that both  $Z_1$  and  $Z_2$  have only real part at the carrier frequency. In practice, load variation and mismatch of circuit parameters may degenerate the resonance, thus  $\eta_{link}$  in Eq. 6 is actually an efficiency upper bound.

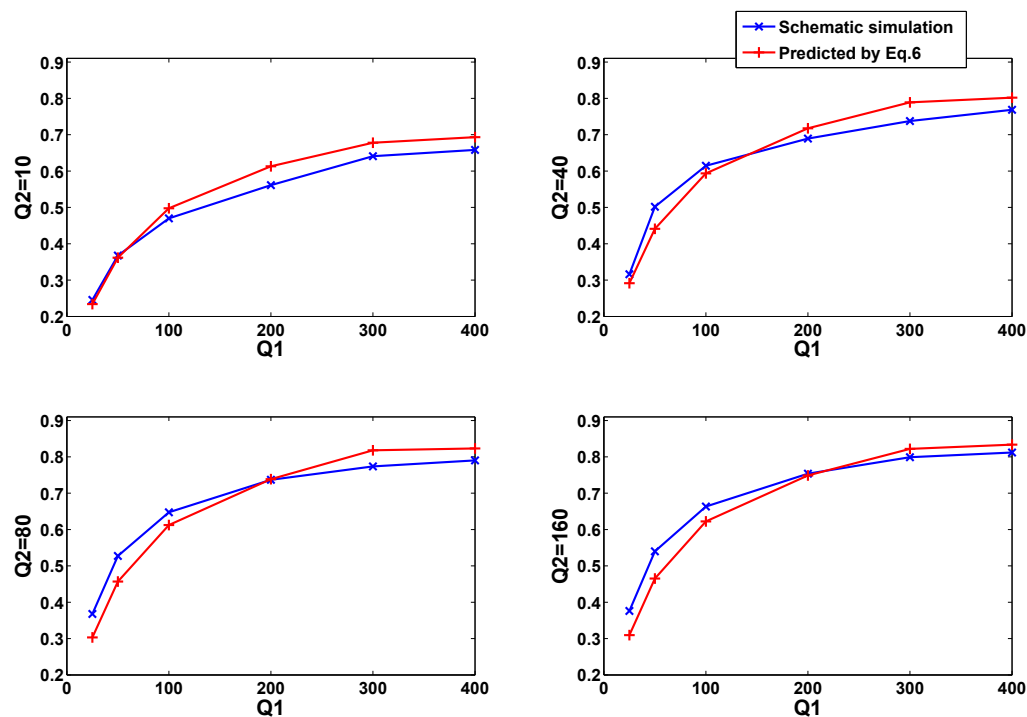


Fig. 5. Power efficiency with different coil quality factor

Note that the power efficiency is a monotonic function of  $X$ , lower  $X$  leads to higher efficiency. A conclusion we drawn from Eq. 6 is that the maximal achievable power efficiency is positively correlated with  $Q$  and coupling coefficient of the coils. It suggests that coils are the most important components for performance optimization. In section 2.4, both prediction based on Eq. 6 and circuit simulation results are given to sketch the function of power efficiency vs. different parameters, confirming above conclusion.

2.4 Simulation verifications

To quantitatively explore power efficiency and its sensitivity to different parameters, numeric simulations are performed and summarized in this section. A first set of simulations are designed to evaluate power efficiency as a function of  $Q$ . The external coil quality factor  $Q_1$  is swept from 25 to 400 and internal coil quality factor  $Q_2$  is swept from 10 to 160. The coupling coefficient  $K$  is set as 0.1 and both internal coil and external coil have 20uH inductance. Table 1 gives power efficiency under different combinations of  $Q_1$  and  $Q_2$ , where a positive correlation between power efficiency and  $Q$  is observed. The simulation results are

$Q_1$	$Q_2 = 10$	$Q_2 = 20$	$Q_2 = 40$	$Q_2 = 80$	$Q_2 = 160$
25	0.24553	0.30505	0.31602	0.36770	0.37608
50	0.36763	0.44904	0.50174	0.52742	0.54013
100	0.46992	0.56561	0.61463	0.64740	0.66343
200	0.56127	0.63658	0.68944	0.73677	0.75357
300	0.64103	0.70081	0.73770	0.77357	0.79913
400	0.65824	0.72009	0.76860	0.79026	0.81193

Table 1. Power efficiency with different coil quality factor



$K$	$Q_1 = 25, Q_2 = 10$	$Q_1 = 25, Q_2 = 160$	$Q_1 = 400, Q_2 = 10$	$Q_1 = 400, Q_2 = 160$
0.01	0.0029	0.0074	0.0417	0.0721
0.04	0.0522	0.0794	0.3844	0.5110
0.07	0.1553	0.2102	0.5878	0.7463
0.10	0.2455	0.3261	0.6582	0.8119
0.13	0.3443	0.4394	0.6984	0.8440
0.16	0.3937	0.5131	0.7184	0.8644
0.20	0.4601	0.5932	0.7296	0.8901

Table 2. Power efficiency with different coupling coefficient

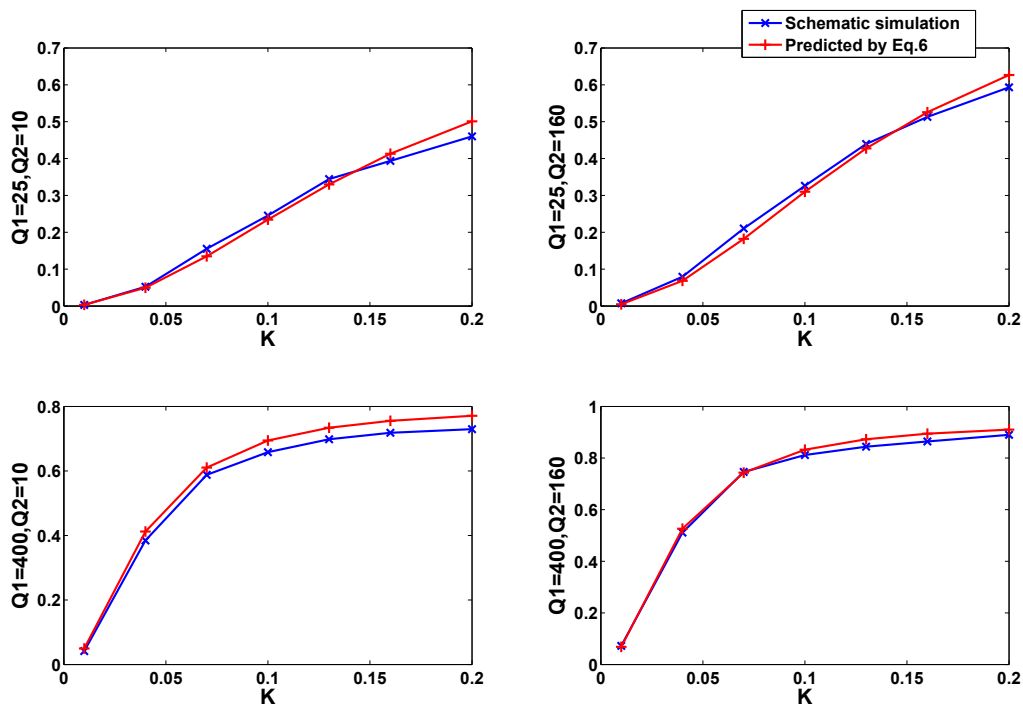


Fig. 6. Power efficiency with different coupling coefficient  $K$

also plotted in Fig. 5 in comparison with analytical results predicted by Eq. 6. High  $Q$  coils can be used to improve power efficiency, however, the realization may violate the constraints on coil geometry size and weight. A critical optimization approach is to increase coil  $Q$  under given geometry and weight constraints, which is the focus of Section 3.

A second set of simulations is designed to evaluate power efficiency as a function of coupling coefficient  $K$ .  $K$  is swept from 0.01 to 0.2 under four combinations of  $Q_1, Q_2$ . The results in Table 2 show that higher coupling coefficient leads to higher power efficiency. In Fig. 6, schematic circuit simulation results are plotted in comparison with the analytical predicted results by Eq. 6, showing a close match. In practice, coupling coefficient is determined by coil separation and coil size, which are fixed parameters in many applications. Consequently, improving the  $Q$  factor of coils is a more practical approach to improve efficiency as shown in Section 3.

### 3. Inductor modeling

When coil operates at low frequency, its  $Q$  factor is defined as  $Q = \frac{\omega L}{R}$ , where  $\omega$  is frequency,  $L$  is inductance, and  $R$  is series resistance. As frequency increases, frequency-related effects including skin effect, proximity effect Berleze & Robert (2003); Chen et al. (1993); Dwight (1945); Egiziano & Vitelli (2004); Lotfi et al. (1992); Murgatroyd (1989); Ravazzani et al. (2002) and self-resonance Massarini & Kazimierczuk (1997) modify both  $L$  and  $R$ , dramatically degenerating the  $Q$  factor. A formula predicting the  $Q$  factor is

$$Q(f) = \frac{2\pi f L}{R} \frac{1 - f^2/f_{self}^2}{1 + f^2/f_h^2}, \quad (7)$$

where  $f_h$  is a parameter to quantify the impact from proximity effect (skin effect) and  $f_{self}$  is coil's self-resonant frequency.  $f_h$  and  $f_{self}$  are expressed by geometry and physical parameters, briefly

$$f_h \propto \frac{1}{r_s^2 \sigma \sqrt{N_t N_s}}, \quad f_{self} \propto \frac{1}{\sqrt{a \ln \frac{a}{r_t} \sum C_{p,k} (k-p)^2}} \quad (8)$$

where  $r_s$ ,  $r_t$ , and  $a$  are the radius of a strand, a turn, and the coil loop (Usually litz winding is used, where one turn contains multiple strands; otherwise,  $r_s = r_t$ ).  $N_s$  and  $N_t$  are the number of strands per turn and the number of turns of the coil winding.  $\sigma$  is the metal conductivity,  $C_{p,k}$  is the parasitic capacitance between turn  $p$  and turn  $k$ .

For any given coil, there is an optimal frequency  $f_{peak}$  that has the maximal  $Q$ . To maximize the power efficiency,  $f_{peak}$ s of the coil pair should be designed in accordance with the power carrier frequency. Based on Eq. 7, an analytical form of  $f_{peak}$  is

$$\frac{1}{f_{peak}^2} \approx \frac{1}{f_h^2} + \frac{3}{f_{self}^2}. \quad (9)$$

Equation 9 represents a key design equation and a closed form analytical solution for  $f_{peak}$ . With this single equation of merit, the maximum  $Q$ , as well as the maximum efficiency of the telemetry system, can be determined. By changing the design parameters, one may tune  $f_{peak}$  close to the target frequency and maximize the power efficiency of the telemetry.

This section is a simplified introduction on inductor modeling basically according to the reference Yang et al. (2007) which has more detailed formula derivations.

#### 3.1 Equivalent AC resistance

In the case that the radius of the cylindrical conductor is smaller or comparable to the skin depth, a first order approximation of Bessel functions allows the calculation of the AC resistance Ferreira (1992); Carter (1967)

$$R_{SK} = R_{DC} [1 + 0.021 (r_s / \delta)^4], \quad (10)$$

where  $r_s$  is the radius of an individual strand,  $R_{DC}$  is the DC resistance, and  $\delta$  is the skin depth  $\delta = \sqrt{2 / \mu_0 \sigma \omega}$ .  $\mu_0$  and  $\sigma$  are the permeability and conductivity of the conductor, respectively. According to Ferreira (1994), the power dissipation from proximity effect in a single strand can be approximated as

$$P_{PRO} = \frac{\pi^3 r_s^4 \mu_0^2 \sigma f^2}{2} H_{peak}^2, \quad (11)$$

where  $H_{peak}$  is the peak  $H$  field through one strand.  
By summarizing  $P_{PRO}$  over all strands, the power dissipation of the coil’s winding from proximity effect is

$$P_{PRO.wind} = \frac{\pi^2 r_s^4 \mu_0^2 \sigma N_t^3 N_s I^2 f^2}{8 A_{winding}} \eta (b/t), \tag{12}$$

where  $A_{winding}$  is the area of the cross section and  $\eta$  is a parameter defined to characterize a coil’s geometry properties. Numeric values of  $\eta$  for different coils are shown in Figure 7.

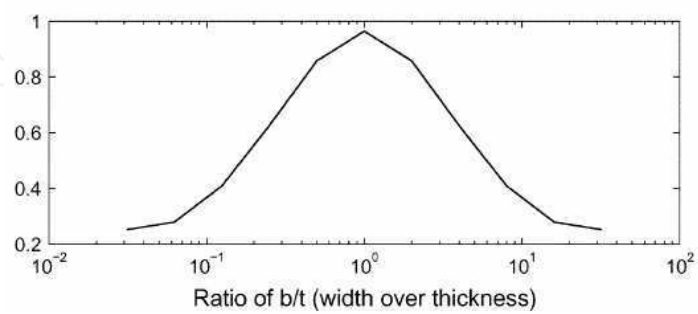


Fig. 7. Numeric values of  $\eta$  for coils with different cross sections.  $b$  and  $t$  are the coil’s width and thickness.

Using Eq. 10 and Eq. 12, the AC resistance of a coil is derived as

$$R_{AC} = R_{DC} \frac{P_{SK.wind} + P_{PRO.wind}}{P_{DC.wind}} = R_{DC} \left(1 + \frac{f^2}{f_h^2}\right), \tag{13}$$

where  $f_h$  is the frequency at which the AC power dissipation is twice the DC power dissipation and expressed as

$$f_h = \frac{2\sqrt{2}}{\pi r_s^2 \mu_0 \sigma \sqrt{N_t N_s \eta \beta}}. \tag{14}$$

3.2 Coil self-resonant frequency

The equivalent distributive network of a coil at high frequency is shown in Figure 8.

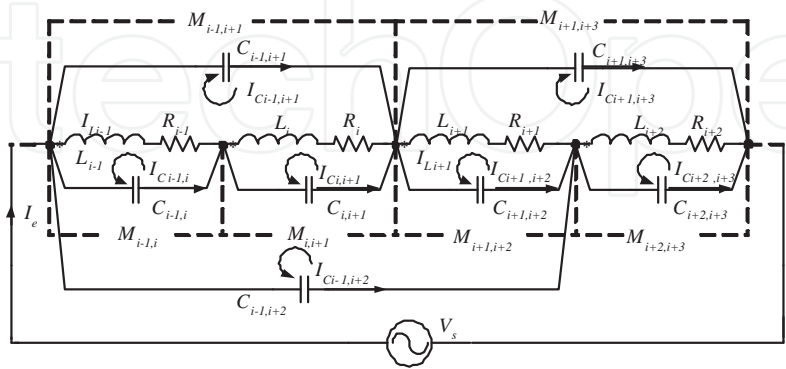


Fig. 8. Distributive equivalent model of a coil.  $I_{L_i}$  represents the current going through the inductive branch  $L_i$ ,  $R_i$  is the equivalent ESR of the inductive branch  $L_i$ ,  $I_{C_{p,k}}$  denotes the mesh current through the parasitic capacitance  $C_{p,k}$ ,  $I_e$  is the external driving current, and  $M_{p,k}$  is the mutual inductance between turn  $p$  and turn  $k$ .

As illustrated in Figure 8, a coil is modeled as a distributive RCL network. Given that the voltage difference between two strands in the same turn is very small compared with the voltage difference between turns, the parasitic capacitance between strands in the same turn can be ignored. Each turn is then modeled as one node with unit inductance and AC resistance. Both inductive and capacitive couplings between turns ( $p$  and  $k$ ) are modeled as mutual inductance  $M_{p,k}$  and parasitic capacitance  $C_{p,k}$ . The analytical expression of the self-inductance of one turn is calculated as Sadiku (1994)

$$L_i = 0.5\mu_0 D_i \ln(D_i/OD), \quad (15)$$

where  $D_i$  is the diameter of the conductor loop and  $OD$  is the diameter of a single turn. Under the assumption that  $OD$  is negligible compared with the diameters of the conductor loops, mutual inductance  $M_{p,k}$  can be calculated by Neumann formula

$$M_{p,k} = \mu_0 \int (\cos\theta/l) ds ds', \quad (16)$$

where  $\theta$  is the angle of inclination between the two loop elements  $ds$  and  $ds'$ ,  $l$  is the radius vector between them, and the integration is to be taken over the contours of the two loops.  $R_i$  is used to model the series resistance of one turn and can be calculated using Eq. 13

$$R_i = \frac{R_{DC}}{N_t} \left(1 + \frac{f^2}{f_h^2}\right). \quad (17)$$

At a coil's self-resonance, the external driving current  $I_e$  reaches its minimum. The corresponding frequency (self-resonant frequency) can be found by solving the network as shown in Fig. 8. To obtain a convenient expression of the currents at different branches, the Mesh theorem is used Dorf (1993). Since the number of independent meshes is equal to the number of parasitic capacitors plus one, which comes from the external driving circuit, we construct the mesh currents based on individual parasitic capacitor.

Denoting the mesh current from node  $p$  to node  $k$  as  $I_{C_{p,k}}$ , and the external driving current as  $I_e$ ,  $I_{L_i}$  is defined as the sum of mesh currents and external driving current

$$I_{L_i} = I_e - \sum_{p \leq i, k \geq i+1} I_{C_{p,k}}. \quad (18)$$

Through the inductive branches, we obtain the voltage difference between node  $p$  and node  $k$  as

$$V_{p,k} = \sum_{p \leq i < k} \omega L_i I_{L_i} + \sum_{p \leq i < k} \sum_{j \neq i} \omega M_{j,i} I_{L_j} + \sum_{p \leq i < k} I_{L_i} R_i, \quad (19)$$

where  $L_i$  is the unit inductance of turn  $i$ ,  $M_{j,i}$  the mutual inductance between turn  $j$  and turn  $i$ , and  $R_i$  the resistance of turn  $i$ , as shown in Fig. 8.

Given that a coil's cross section is much smaller than the area of the conductor loop ( $b \ll D_{out}$ ,  $t \ll D_{out}$ ), the coupling coefficient between two turns is close to 1. Therefore, Eq. 19 is simplified by assuming that the flux ( $\Phi_{unit}$ ) going through any individual turn is the same. Flux ( $\Phi_{unit}$ ) can be defined as

$$\begin{aligned} \Phi_{unit} &= \sum_{i=1}^{N_t} L_i I_{L_i} = I_e \sum_{i=1}^{N_t} L_i - \sum_{i=1}^{N_t} L_i \sum_{p \leq i, k \geq i+1} I_{C_{p,k}} \\ &\approx N_t L_i I_e - L_i \sum_{p < k} I_{C_{p,k}} (k - p), \end{aligned} \quad (20)$$

where  $N_t$  is the number of turns. As a result, the voltage difference between node  $p$  and node  $k$  becomes

$$V_{p,k} = \omega(k-p)\Phi_{unit}\angle 90^\circ + R_i \sum_{p \leq i < k} I_{L_i}. \quad (21)$$

Alternatively, the voltage difference can be computed through the capacitive branches as

$$V_{p,k} = \frac{I_{C_{p,k}} \angle -90^\circ}{\omega C_{p,k}}, \quad (22)$$

where  $C_{p,k}$  is the parasitic capacitance between turn  $p$  and turn  $k$ . Equation 21 and 22 are combined to give the following expression for the mesh current  $I_{C_{p,k}}$  as

$$I_{C_{p,k}} = -\omega^2 C_{p,k}(k-p)\Phi_{unit} + \omega R_i C_{p,k} \angle 90^\circ \sum_{p \leq i < k} I_{L_i}. \quad (23)$$

To obtain a direct relationship between external driving current  $I_e$  and frequency, using the sum of  $(k-p)I_{C_{p,k}}$ , the resulting equation is

$$\sum_{p < k} (k-p)I_{C_{p,k}} = -\omega^2 \Phi_{unit} \sum_{p < k} C_{p,k}(k-p)^2 + \omega R_i \angle 90^\circ \sum_{p < k} C_{p,k}(k-p) \sum_{p \leq i < k} I_{L_i}. \quad (24)$$

Substituting 20 into 24 yields

$$\frac{1}{1-\alpha} = \omega^2 L_i \sum_{p < k} C_{p,k}(k-p)^2 - \omega R_i \angle 90^\circ \sum_{p < k} C_{p,k}(k-p), \quad (25)$$

where

$$\alpha = \frac{N_t I_e}{\sum_{p < k} I_{C_{p,k}}(k-p)}. \quad (26)$$

The solution to Eq. 25 is

$$\omega_{self} = \frac{A \pm B}{G}, \quad (27)$$

where

$$A = R_i \angle 90^\circ \sum_{p < k} C_{p,k}(k-p)$$

$$B = \sqrt{\frac{1}{1-\alpha} 4L_i \sum_{p < k} C_{p,k}(k-p)^2 - R_i^2 [\sum_{p < k} C_{p,k}(k-p)]^2}$$

$$G = 2L_i \sum_{p < k} C_{p,k}(k-p)^2.$$

To provide a simplified formula to predict the self-resonant frequency, additional approximations are made (a)  $\alpha \approx 0$ ; (b)  $4L_i \sum_{p < k} C_{p,k}(k-p)^2 \gg R_i^2 [\sum_{p < k} C_{p,k}(k-p)]^2$ . Consequently, the self-resonant frequency  $f_{self}$  can be calculated as Bartoli et al. (1996)

$$f_{self} = \frac{1}{2\pi \sqrt{LC_{self}}}, \quad (28)$$

where

$$L = N_t^2 L_i, C_{self} = \sum_{p < k} C_{p,k}(k-p)^2 / N_t^2. \quad (29)$$

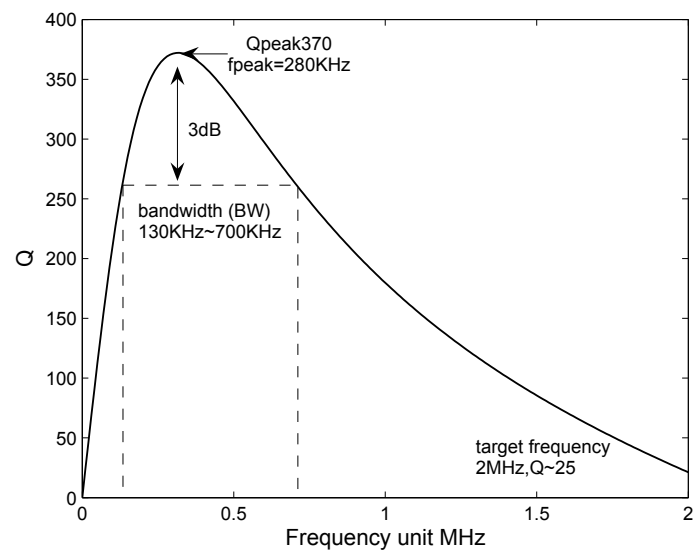


Fig. 9. Q vs Frequency curve. Coil specifications:  
 $N_t = 50, N_s = 30, D_{out} = 4.0cm, D_{in} = 2.8cm, r_s = 25um, L = 110uH, R_{DC} = 0.30ohm$ .

3.3 Quality factor

Using lumped circuit model suggested by Eq. 28 and 29, the equivalent impedance of a coil considering  $C_{self}$  is

$$Z_e = (j\omega L + R_{AC}) \parallel \frac{1}{j\omega C_{self}} = \frac{R_{AC} + j\omega L}{(1 - \omega^2 LC_{self}) + j\omega R_{AC} C_{self}}. \tag{30}$$

The Q of a coil with impedance given in Eq. 30 is

$$Q(f) \approx 2\pi f L (1 - \frac{f^2}{f_{self}^2}) / R_{DC} (1 + \frac{f^2}{f_h^2}), \tag{31}$$

where  $f_h = 2\sqrt{2}/(\pi r_s^2 \mu_0 \sigma \sqrt{\eta \beta N_t N_s})$ ,  $f_{self}^{-1} = 2\pi \sqrt{LC_{self}}$  and  $R_{DC} = N_t(D_{out} + D_{in})/2\sigma \pi r_s^2 N_s$ , as defined previously.

A typical curve to characterize the Q of a coil is shown in Figure 9.  $f_{peak}$  represents the frequency at which a coil has the maximum Q, denoted as  $Q_{peak}$ . For telemetries, the power transfer efficiency and the heat dissipation are the primary concerns, therefore it is desirable to have the coil operating near  $f_{peak}$ .

Taking the derivative of the Q and setting it to zero allows the derivation of  $f_{peak}$ .  $f_{peak}$  is approximately given as

$$f_{peak}^2 \approx f_h^2 \parallel \frac{f_{self}^2}{3} \tag{32}$$

Equation 32 represents a key design equation, and a closed form analytical solution for  $f_{peak}$ . With this single equation of merit, the bandwidth(BW) and the maximum Q, and as well as the maximum efficiency of the telemetry system, can be determined. By changing the design parameters, one may tune  $f_{peak}$  close to the target frequency and maximize the power efficiency of the telemetry.

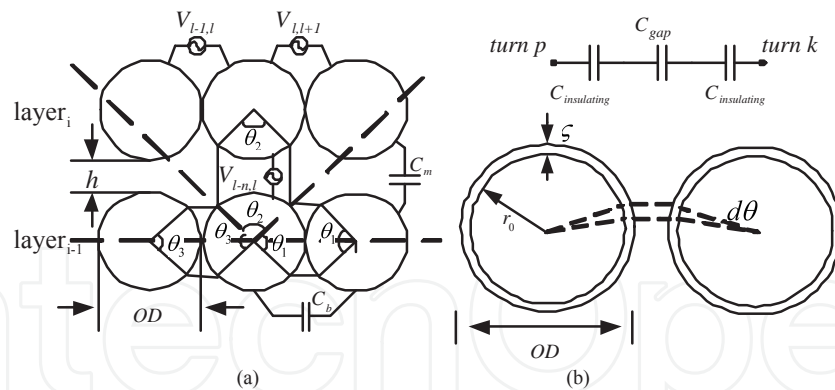


Fig. 10. Turn-to-turn parasitic capacitance. (a) Illustration of the parasitic capacitance in a coil winding. (b) Equivalent model to calculate the turn-to-turn parasitic capacitance.

### 3.4 Turn-to-turn parasitic capacitance

The cross section of a multiple-layer coil is shown in Figure 10, where  $C_m$  denotes the parasitic capacitance between turns in different layers,  $C_b$  the parasitic capacitance between turns in the same layer, and  $\theta_i$  ( $i = 1, 2, 3$ ) is the effective angle between two turns. As illustrated in Figure 10(b), the turn-to-turn parasitic capacitance is a combination of parasitic capacitances through the insulation layer and the nonconductive gap.

The parasitic capacitance contributed by the dielectric insulating layer per unit angle is Massarini et al. (1996)

$$C_{insulate} = \frac{\epsilon_0 \epsilon_r \pi D_i}{\ln \frac{r_0}{r_0 - \zeta}}, \quad (33)$$

where  $\zeta$  is the thickness of the insulation layer,  $r_0$  the radius of a single turn and  $D_i$  the average diameter of the conductor loop.

Assuming the dielectric constant of the gap is  $\epsilon_0$ , the parasitic capacitance contributed by the gap per unit angle is approximately computed by

$$C_{gap} = \frac{\epsilon_0 \pi D_i}{2(1 - \cos \theta) + \frac{h}{r_0}}, \quad (34)$$

where  $h$  is the separation between two turns.

As a result, the total parasitic capacitance per unit angle is approximated as

$$C_t = \frac{0.5 C_{gap} C_{insulate}}{C_{gap} + 0.5 C_{insulate}}. \quad (35)$$

Under the condition that  $\zeta \ll r_0$ , the parasitic capacitance between two turns is

$$C_{p,k} = \epsilon_0 \epsilon_r \int_0^{\theta_e/2} \frac{\pi D_i r_0}{\zeta + \epsilon_r r_0 (1 - \cos \theta) + 0.5 \epsilon_r h} d\theta, \quad (36)$$

where  $\theta_e$  is the effective angle between turn  $p$  and turn  $k$ .

As a first order approximation, assume that each turn except those on the perimeter of a coil is surrounded by four turns and  $\theta_1 = \theta_2 = \theta_3 = 90^\circ$ .



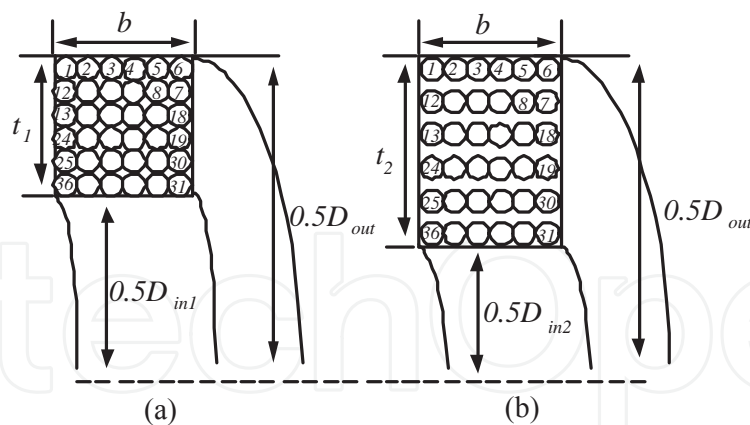


Fig. 11. Coils' cross sections. (a) Coil "I", tightly wound litz coil. (b) Coil "II", loosely wound litz coil with separation between layers.

#### 4. Design examples

In this section, examples to illustrate the tradeoff between coil design parameters,  $f_{peak}$  and the  $Q$  are presented. Since the outer diameter, thickness, and inductance of a coil are typically specified for biomedical applications, design parameters available for optimization are the inner diameter, winding sequence, the number of strands per turn, and the diameter of an individual strand.

##### 4.1 Inner diameter

When the target frequency is a few MHz or higher, a major design concern is the self-resonant frequency. To increase the self-resonant frequency of a coil and thus  $f_{peak}$ , an effective and practical method is to reduce a coil's inner diameter and increase the separation between layers, as shown in Fig. 11

According to Eq. 29, a general expression for the total parasitic capacitance for both coil I and "II", as illustrated in Fig. 11, is

$$C_{self} = \frac{1}{N_t^2} [C_b(l-1)m + C_m \sum_{i=1}^l (2i-1)^2(m-1)], \quad (37)$$

where  $C_b$  is the parasitic capacitance between two nearby turns in the same layer and  $C_m$  the parasitic capacitance between different layers, as shown in Figure 10.

For a tightly wound coil, e.g., coil "I", the parasitic capacitance between two nearby turns other is

$$C_b = C_m = \epsilon_0 \epsilon_r \int_0^{\frac{\pi}{4}} \frac{\pi D_i r_0}{\zeta + \epsilon_r r_0 (1 - \cos \theta)} d\theta \quad (38)$$

For coils with spacing between layers, e.g., coil "II", the parasitic capacitance is

$$\begin{cases} C_b = \epsilon_0 \epsilon_r \int_0^{\frac{\pi}{4}} \frac{\pi D_i r_0}{\zeta + \epsilon_r r_0 (1 - \cos \theta)} d\theta \\ C_m = \epsilon_0 \epsilon_r \int_0^{\frac{\pi}{4}} \frac{\pi D_i r_0}{\zeta + \epsilon_r r_0 (1 - \cos \theta) + 0.5 \epsilon_r h} d\theta, \end{cases} \quad (39)$$

where  $h$  is the separation between two layers.



Coil	$D_{in}$	$C_b$	$C_m$	$L$	$C_{self}$	$f_{self}$
$I, h = 0$	$2.76cm$	$15pF$	$15pF$	$85uH$	$17pF$	$4.1MHz$
$II, h = r_0$	$2.66cm$	$15pF$	$1.0pF$	$77uH$	$1.5pF$	$15MHz$

Table 3. Parasitic capacitance, self-resonant frequency of coil "I" and "II". Coil Specifications:  $D_{out} = 3cm, OD = 200um, h = 100u, \zeta = 3um, \epsilon_r = 3$ .

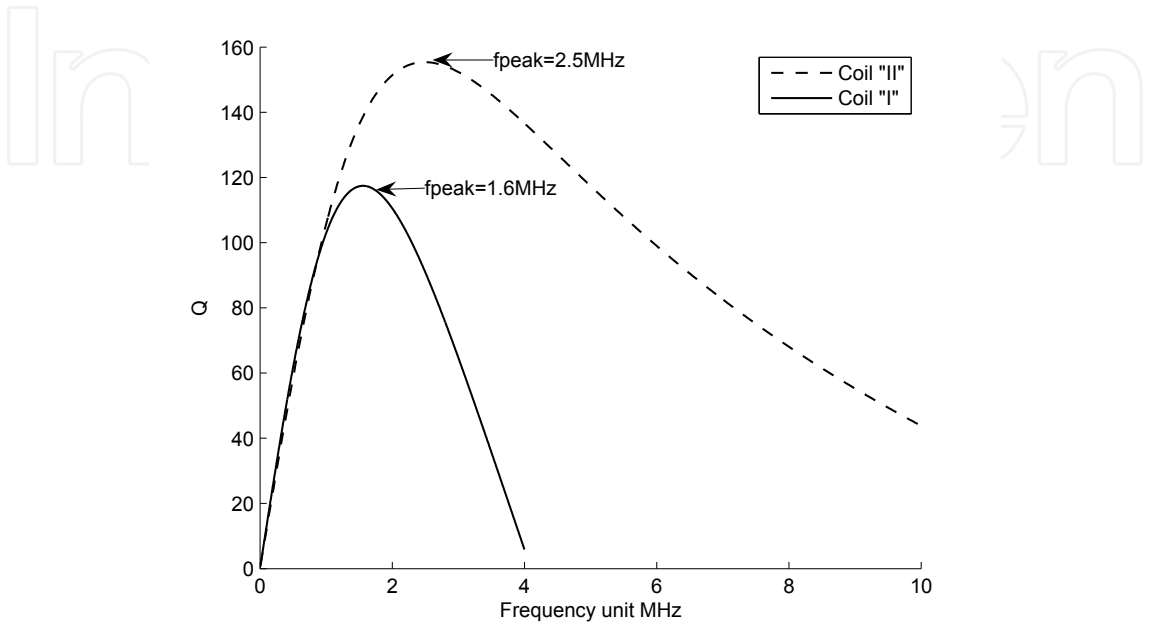


Fig. 12. Q vs Frequency curves of coil "I" and "II".

Using proposed formulae, the total parasitic capacitance and the self-resonant frequency can be calculated directly. An example of the result is shown in Table 3.

As shown in Table 3, Coil "I" and "II" have similar geometry parameters, inductances, and DC resistances. The only difference between them is that coil "II" has an additional air gap between two layers. In practical coil design, such a gap can be achieved by increasing the bundle level insulation coating. The values in the last column of Table II demonstrate that coils with spacing between layers (e.g., Coil "II") have a much higher self-resonant frequency than tightly wound coils (e.g., Coil "I"). As a result of layer to layer spacing, the inner diameter of coil "II" is reduced to  $2.66cm$ , while the inner diameter of coil "I" is  $2.76cm$ . The Q vs Frequency curves for both coil "I" and "II" are shown in Fig. 12, assuming AWG44, 7 strand litz wire ( $OD = 200\text{ }\mu m$ ) is used to wind the coils.

As Fig. 12 illustrates, at low frequencies, the Q for both coil "I" and "II" are similar. This is because the frequency of operation is well below the self-resonant frequency and the AC power dissipation is close to the DC power dissipation. At higher frequencies, coil "II" has a higher Q than coil "I", mainly due to lower parasitic capacitance.

4.2 Winding sequence

The winding sequence of the turns of a coil also affects the total parasitic capacitance and the self-resonant frequency. Two coils with the same geometry parameters but different winding sequences are shown in Fig. 13.

In Fig. 13, the numbers in the wire cross section indicate the winding sequence. The total parasitic capacitance for coil "III", due to the altered winding sequence is expressed as

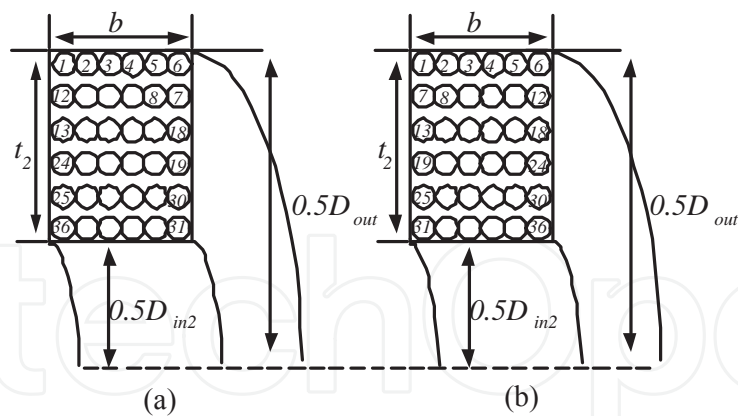


Fig. 13. Coils’ cross sections. (a) Coil "II", loosely wound litz coil with normal winding sequence and separation between layers. (b) Coil "III", loosely wound litz coil with different winding sequence and separation between layers.

$$C_{self} = \frac{1}{N_t^2} [C_b(l - 1)m + C_m l^3(m - 1)]$$

(40)

Coil	$C_b$	$C_m$	$L$	$C_{self}$	$f_{self}$
II, $h = OD/2$	15pF	1.0pF	77uH	1.5pF	15MHz
III, $h = OD/2$	15pF	1.0pF	77uH	1.2pF	17MHz

Table 4. Parasitic capacitance, self-resonant frequency of coil "II" and "III". Coil Specifications:  $D_{out} = 3cm, D_{in} = 2.66cm, OD = 200um, h = 100u, \zeta = 3um, \epsilon_r = 3$ .

4.3 The number of strands

If the cross section of the winding is fixed, reducing the number of strands is an effective way to increase  $f_{peak}$  and the Q at higher frequencies for two reasons. First,  $f_{self}$  increases, due to the increased separation between nearby turns, as shown in Fig. 14. Second,  $f_h$  increases, since the total number of strands in the winding decreases. Therefore, both  $f_{peak}$  and the Q are larger at higher frequencies. For the purpose of demonstration, numeric comparisons of several coils with different geometry parameters are given in Table 5.

Coil	$N_s$	$R_{DC}$	$f_{self}$	$f_{peak}$	$Q_{peak}$	BW (bandwidth)
IV	3	9.5ohm	26MHz	8.5MHz	198	2.5 – 15.5MHz
V	7	4.1ohm	19MHz	4.2MHz	215	1.8 – 8.5MHz
VI	15	1.9ohm	14MHz	2.1MHz	222	0.9 – 4.5MHz
VII	30	0.95ohm	5.6Mhz	1.1MHz	219	0.4 – 2.2MHz

Table 5. Self-resonant frequency, quality factor, bandwidth of coil "IV"-"VII". Coil Specifications:  $D_{out} = 3.2cm, D_{in} = 2.7cm, b = 2.5cm, t = 2.5mm, d_s = 50um, N_t = 36, \zeta = 3um, \epsilon_r = 3, AWG44$ .

The Q vs Frequency curves of coils in Table 5 are plotted in Fig. 15. Even though the DC resistance of a coil is much higher when fewer strands are used per winding, the  $f_{peak}$  and  $f_{self}$  increase significantly. Since telemetry efficiency is a function of the operating frequency, the coil with fewer strands represents a significant improvement compared with conventional implant telemetry design.

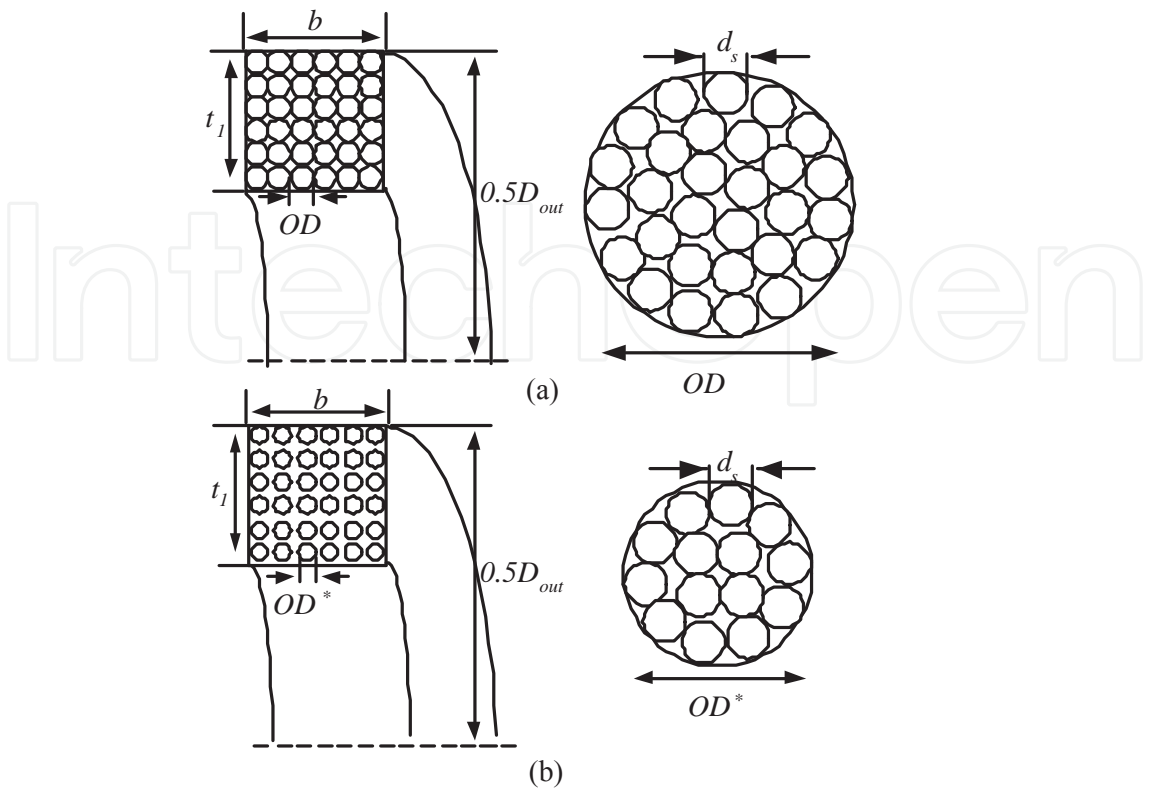


Fig. 14. Coils' cross sections. (a) Tightly wound litz coil with the maximum number of strands. (b) Loosely wound litz coil with less strands.

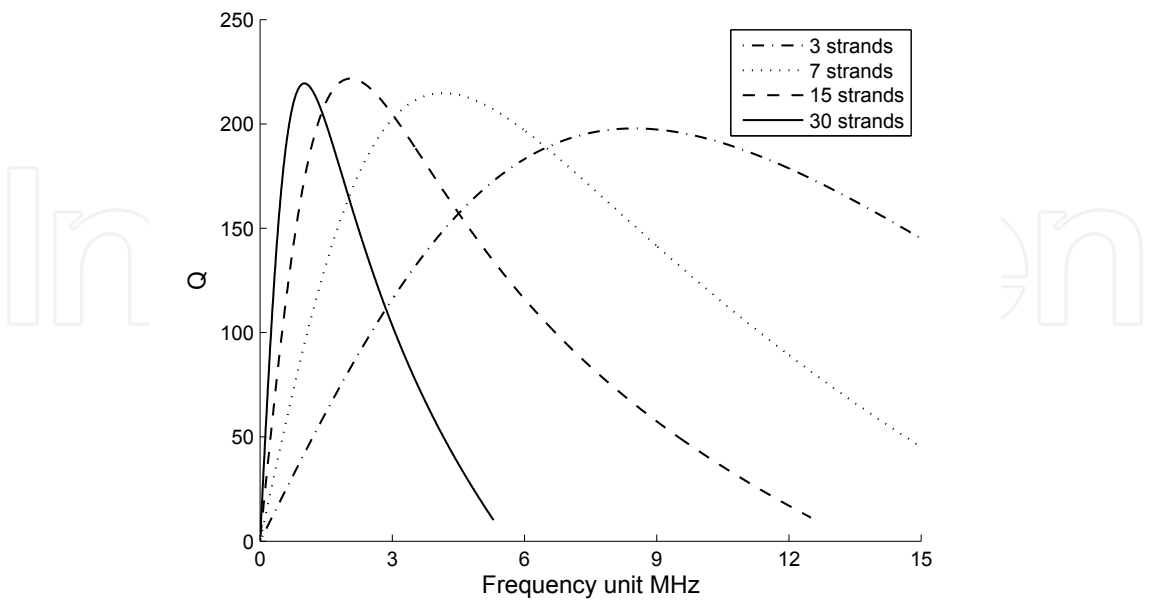


Fig. 15.  $Q$  vs Frequency curves for coils with the same cross sections but different numbers of strands.

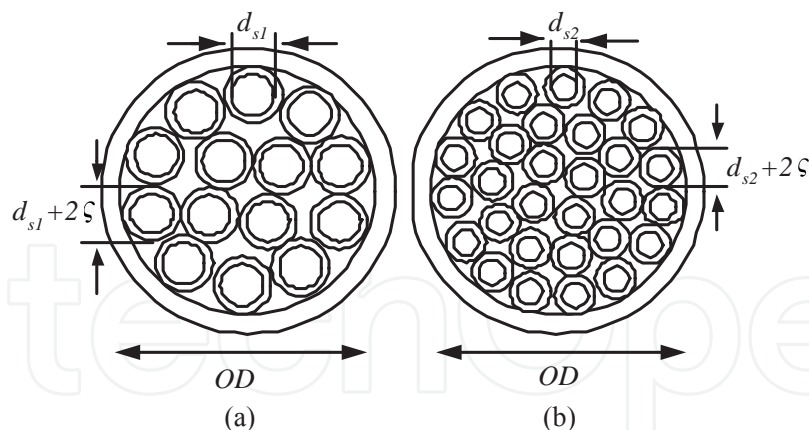


Fig. 16. Cross sections of individual turns. (a) Bigger wire is used. (b) Smaller wire is used.

#### 4.4 Diameter of single strand

Under the assumption that a coil's cross section, inductance, and area efficiency are fixed, the only method to reduce the power consumption from proximity effect is to decrease the size of a single strand and keep the  $OD$  unchanged, as shown in Fig. 16.

If the displaced current is not a concern, a reduction of wire size helps to reduce the power dissipation from proximity effect. Reduction of the wire size is limited in practical coil design for several reasons.

First, once the target frequency is lower than  $f_h$ , the power dissipation from proximity effect is less than the DC power dissipation, thus a further decrease of  $r_s$  only slightly reduces the AC power dissipation.

Second, given the thickness of coating, cross section and inductance, reducing the size of a single strand inevitably decreases area efficiency of an individual strand, thus increasing the DC power dissipation.

Third, experimental results show that an increase of the number of strands increases strand-level displaced currents hence reduces the self-resonant frequency of a coil [Bartoli et al. (1996)].

Fourth, small wire is more expensive.

When  $f_h$  is equal to or greater than the target frequency, power dissipation from proximity effect should not be a major concern.

For coils used in an inductive link, the  $Q$  and  $f_{self}$  are critical. Using the assumption that coils are restricted to a particular geometry set, an analytical closed form solution is derived to determine the  $Q$  and  $f_{self}$ . Not only providing a close form solution, our derivation also allows the designer to set criticality on parameters and find an optimal solution.

## 5. References

- Atluri, S. & Ghovanloo, M. (2005). Design of a wideband power-efficient inductive wireless link for implantable biomedical devices using multiple carriers, *Proceedings of the 2nd International IEEE EMBS Conference on Neural Engineering*, pp. 533–537.
- Baker, M. & Sarpeshkar, R. (2007). Feedback analysis and design of RF power links for low-power bionic systems, *IEEE Transactions on Biomedical Circuits and Systems* 1(1): 28–38.

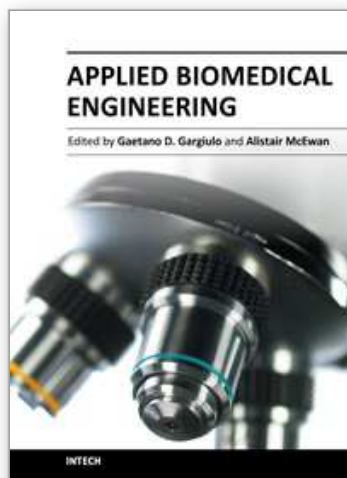
- Bartoli, M., Noferi, N., Reatti, A. & Kazimierczuk, M. (1996). Modeling litz-wire winding losses in high-frequency power inductors, *IEEE Power Electronics Specialists Conference (PESC)*, pp. II: 1690–1696.
- Berleze, S. & Robert, R. (2003). Skin and proximity effects in nonmagnetic conductors, *IEEE Transactions on Education* 46(3): 368–372.
- Carter, G. (1967). *The electromagnetic field in its engineering aspects*, Longman.
- Chaimanonart, N., Olszens, K., Zimmerman, M., Ko, W. & Young, D. (2006). Implantable RF power converter for small animal in vivo biological monitoring, *International Conference of the Engineering in Medicine and Biology Society(EMBS)*, IEEE, pp. 5194–5197.
- Chen, Q., Konrad, A. & Biringer, P. (1993). A hybrid approach to the solution of open boundary eddy current problems under tm field excitation, *IEEE Transactions on Magnetics* 29(6): 2485–2487.
- Chen, Q., Wong, S., Tse, C. & Ruan, X. (2009). Analysis, design, and control of a transcutaneous power regulator for artificial hearts, *IEEE Transactions on Biomedical Circuits and Systems* 3(1): 23–31.
- Dorf, R. (1993). *The Electrical Engineering Handbook*, CRC Press, Boca Raton.
- Dwight, H. (1945). *Electrical Coils and Conductors*, New York: McGraw-Hill.
- Egiziano, L. & Vitelli, M. (2004). Time-domain analysis of proximity effect current driven problems, *IEEE Transactions on Magnetics* 40(2): I: 379–383.
- Ferreira, J. (1992). Analytical computation of ac resistance of round and rectangular litz wire windings, *IEEE Proceedings of Electric Power Applications, Part B* 139(1): 21–25.
- Ferreira, J. (1994). Improved analytical modeling of conductive losses in magnetic components, *IEEE Transactions on Power Electronics* 9(1): 127–131.
- Galbraith, D., Soma, M. & White, R. (2007). A Wide-band efficient inductive transdennal power and data link with coupling insensitive gain, *IEEE Transactions on Biomedical Engineering* 34(4): 265–275.
- Hamici, Z., Itti, R. & Champier, J. (1996). A high-efficiency power and data transmission system for biomedical implanted electronic devices, *Measurement Science and Technology* 7(2): 192–201.
- Harrison, R. (2007). Designing efficient inductive power links for implantable devices, *IEEE International Symposium on Circuits and Systems(ISCAS)*, IEEE, pp. 2080–2083.
- Heller, A. (2006). Potentially implantable miniature batteries, *Analytical and Bioanalytical Chemistry* 385(3): 469–473.
- Kazimierczuk, M. & Jozwik, J. (2002). Resonant dc/dc converter with class-E inverter and class-E rectifier, *Industrial Electronics, IEEE Transactions on* 36(4): 468–478.
- Kendir, G., Liu, W., Bashirullah, R., Wang, G., Humayun, M. & Weiland, J. (2004). An efficient inductive power link design for retinal prosthesis, *Proceedings of the 2004 International Symposium on Circuits and Systems(ISCAS)*, Vol. 4, IEEE.
- Kendir, G., Liu, W., Wang, G., Sivaprakasam, M., Bashirullah, R., Humayun, M. & Weiland, J. (2005). An optimal design methodology for inductive power link with class-E amplifier, *IEEE Transactions on Circuits and Systems I: Regular Papers* 52(5): 857–866.
- Knutson, J., Naples, G., Peckham, P. & Keith, M. (2002). Electrode fracture rates and occurrences of infection and granuloma associated with percutaneous intramuscular electrodes in upper-limb functional electrical stimulation applications, *Journal of Rehabilitation Research and Development* 39(6): 671–684.

- Ko, W., Liang, S. & Fung, C. (1977). Design of radio-frequency powered coils for implant instruments, *Medical and Biological Engineering and Computing* 15(6): 634–640.
- Krauss, H., Bostian, C. & Raab, F. (1980). *Solid state radio engineering*, Wiley New York.
- Li, W., Rodger, D., Weiland, J., Humayun, M. & Tai, Y. (2005). Integrated flexible ocular coil for power and data transfer in retinal prostheses, *International Conference of the Engineering in Medicine and Biology Society (EMBS)*, pp. 1028–1031.
- Liu, W., Vichienchom, K., Clements, M., DeMarco, S., Hughes, C., McGucken, E., Humayun, M., De Juan, E., Weiland, J. & Greenberg, R. (2000). A neuro-stimulus chip with telemetry unit for retinal prosthetic device, *IEEE Journal of Solid-State Circuits* 35(10): 1487–1497.
- Lotfi, A., Gradzki, P. & Lee, F. (1992). Proximity effects in coils for high frequency power applications, *IEEE Transactions on Magnetics* 28(5): II: 2169–2171.
- Massarini, A. & Kazimierczuk, M. (1997). Self-capacitance of inductors, *IEEE Transactions on Power Electronics* 12(4): 671–676.
- Massarini, A., Kazimierczuk, M. & Grandi, G. (1996). Lumped parameter models for single- and multiple-layer inductors, *IEEE Power Electronics Specialists Conference (PESC)*, pp. I: 295–301.
- Murgatroyd, P. (1989). Calculation of proximity losses in multistranded conductor bunches, *IEE Proceedings, Part A, Science, Measurement and Technology* 136(3): 115–120.
- Raab, F. (1977). Idealized operation of the class E tuned power amplifier, *IEEE Transactions on Circuits and Systems* 24(12): 725–735.
- Raab, F. (2002). Class-E, class-C, and class-F power amplifiers based upon a finite number of harmonics, *IEEE Transactions on Microwave Theory and Techniques* 49(8): 1462–1468.
- Ravazzani, P., Ruohonen J., Tognola, G., Anfonso, F., Ollikainen, M., Ilmoniemi, R. & Grandori, F. (2002). Frequency-related effects in the optimization of coil for magnetic stimulation of nervous system, *IEEE Transactions on Biomedical Engineering* 49(5): 463–471.
- Rogers, J. & Plett, C. (2010). *Radio frequency integrated circuit design*, Artech House Publishers.
- Sadiku, N. (1994). *Elements of Electromagnetics*, Orlando, FL: Sounders College Press.
- Sauer, C., Stanacevic, M., Cauwenberghs, G. & Thakor, N. (2005). Power harvesting and telemetry in cmos for implanted devices, *IEEE Transactions on Circuits and Systems I* 52(12): 2605–2613.
- Sivaprakasam, M., Liu, W., Humayun, M. & Weiland, J. (2005). A variable range bi-phasic current stimulus driver circuitry for an implantable retinal prosthetic device, *IEEE Journal of Solid-State Circuits* 40(3): 763–771.
- Smith, B., Tang, Z., Johnson, M., Pourmehdi, S., Gazdik, M., Buckett, J. & Peckham, P. (2002). An externally powered, multichannel, implantable stimulator-telemeter for control of paralyzed muscle, *Biomedical Engineering, IEEE Transactions on* 45(4): 463–475.
- Sokal, N. (2001). Class-E RF power amplifiers, *QEX [published by American Radio Relay League, 225 Main St., Newington, CT 06111-1494, USA], Issue 204: 9–20.*
- Takura, T., Somekawa, T., Sato, F., Matsuki, H. & Sato, T. (2006). Improvement of communication area for implantable signal transmission system with ferrite chip core, *Journal of Applied Physics* 99.
- Theogarajan, L. & Wyatt, J. (2006). Minimally invasive retinal prosthesis, *IEEE International Solid-State Circuits Conference (ISSCC)*, pp. 54–55.



- Wang, G., Liu, W., Sivaprakasam, M. & Kendir, G. (2005). Design and analysis of an adaptive transcutaneous power telemetry for biomedical implants, *IEEE Transactions on Circuits and Systems I: Regular Papers* 52(10): 2109–2117.
- Wang, G., Liu, W., Sivaprakasam, M., Weiland, J. & Humayun, M. (2005). High efficiency wireless power transmission with digitally configurable stimulation voltage for retinal prosthesis, *International Conference of the Engineering in Medicine and Biology Society (EMBS)*, pp. 543–546.
- Yang, Z., Liu, W. & Basham, E. (2007). Inductor modeling in wireless links for implantable electronics, *IEEE Transactions on Magnetics* 43(10): 3851–3860.
- Zierhofer, C. & Hochmair, E. (2002). High-efficiency coupling-insensitive transcutaneous power and data transmission via an inductive link, *IEEE Transactions on Biomedical Engineering* 37(7): 716–722.

IntechOpen



## **Applied Biomedical Engineering**

Edited by Dr. Gaetano Gargiulo

ISBN 978-953-307-256-2

Hard cover, 500 pages

**Publisher** InTech

**Published online** 23, August, 2011

**Published in print edition** August, 2011

This book presents a collection of recent and extended academic works in selected topics of biomedical technology, biomedical instrumentations, biomedical signal processing and bio-imaging. This wide range of topics provide a valuable update to researchers in the multidisciplinary area of biomedical engineering and an interesting introduction for engineers new to the area. The techniques covered include modelling, experimentation and discussion with the application areas ranging from bio-sensors development to neurophysiology, telemedicine and biomedical signal classification.

### **How to reference**

In order to correctly reference this scholarly work, feel free to copy and paste the following:

Kejie Huang, Yin Zhou, Xiaobo Wu, Wentai Liu and Zhi Yang (2011). Design and Optimization of Inductive Power Link for Biomedical Applications, Applied Biomedical Engineering, Dr. Gaetano Gargiulo (Ed.), ISBN: 978-953-307-256-2, InTech, Available from: <http://www.intechopen.com/books/applied-biomedical-engineering/design-and-optimization-of-inductive-power-link-for-biomedical-applications>

**INTech**  
open science | open minds

### **InTech Europe**

University Campus STeP Ri  
Slavka Krautzeka 83/A  
51000 Rijeka, Croatia  
Phone: +385 (51) 770 447  
Fax: +385 (51) 686 166  
[www.intechopen.com](http://www.intechopen.com)

### **InTech China**

Unit 405, Office Block, Hotel Equatorial Shanghai  
No.65, Yan An Road (West), Shanghai, 200040, China  
中国上海市延安西路65号上海国际贵都大饭店办公楼405单元  
Phone: +86-21-62489820  
Fax: +86-21-62489821



© 2011 The Author(s). Licensee IntechOpen. This chapter is distributed under the terms of the [Creative Commons Attribution-NonCommercial-ShareAlike-3.0 License](https://creativecommons.org/licenses/by-nc-sa/3.0/), which permits use, distribution and reproduction for non-commercial purposes, provided the original is properly cited and derivative works building on this content are distributed under the same license.

IntechOpen

IntechOpen